# Biaxial Deformation of the Magnesium Alloy AZ80

P. TOMLINSON, H. AZIZI-ALIZAMINI, W.J. POOLE, C.W. SINCLAIR, and M.A. GHARGHOURI

The multiaxial deformation of magnesium alloys is important for developing reliable, robust models for both the forming of components and also analysis of in-service performance of structures, for example, in the case of crash worthiness. The current study presents a combination of unique biaxial experimental tests and biaxial crystal plasticity simulations using a visco-plastic self-consistent (VPSC) formulation conducted on a relatively weak AZ80 cast texture. The experiments were conducted on tubular samples which are loaded in axial tension or compression along the tube and with internal pressure to generate hoop stresses orthogonal to the axial direction. The results were analyzed in stress and strain space and also in terms of the evolution of crystallographic texture. In general, it was found that the VPSC simulations matched well with the experiments. However, some differences were observed for cases where basal $\langle a \rangle$ slip and $\{10\bar{1}2\}$ extension twinning were in close competition such as in the biaxial tension quadrant of the plastic potential. The evolution of texture measured experimentally and predicted from the VPSC simulations was qualitatively in good agreement. Finally, experiments and VPSC simulations were conducted on a second AZ80 material which had a stronger initial texture and a higher level of mechanical anisotropy. In the previous case, the agreement between experiments and simulations was good, but a larger difference was observed in the biaxial tension quadrant of the plastic potential.

DOI: 10.1007/s11661-013-1707-x


## I. INTRODUCTION

OVER the past several years, there has been a resurgence of interest to characterize and model the fundamental deformation behavior of hexagonal close packed (HCP) metals,[1] in particular magnesium. (see the recent reviews[2,3]). The basic framework for understanding the deformation behavior of magnesium and its alloys has been developed, but it is complex. The slip modes of primary interest in magnesium are basal $\langle a \rangle$, prism $\langle a \rangle$ and second-order pyramidal $\langle c+a \rangle$, while deformation by twinning can occur by extension twins $\{10\bar{1}2\}$ or contraction twins $\{10\bar{1}1\}$; there also exists various possible double-twinning scenarios.[3,4] In general, it is accepted that nonbasal slip is significantly more difficult compared with basal slip and that extension twinning is much easier than contraction twinning. General arbitrary deformation of polycrystalline samples requires a complex combination of these basic deformation modes.[5] Further, it is well recognized that crystallographic texture assumes a critical role in the deformation of polycrystal samples. The interplay between grain orientation, its local neighbourhood, and the applied stress field stress will determine which of the deformation modes will be active to accommodate the far-field deformation. The local response when averaged over all crystals is manifest in the macroscopic behavior where very significant anisotropy and dependence on stress state (*e.g.*, the tension/compression asymmetry) are often observed.

This complexity generally requires the use of crystal plasticity models to interpret the macroscopic behavior. The most commonly used crystal plasticity modeling tools for predicting the behavior of magnesium are the so-called mean field models. These include the elasto-plastic self-consistent (EPSC[6,7]), visco-plastic self-consistent (VPSC[8,9]), and elastic-viscoplastic self-consistent (EVPSC[10]) models although recent study has also seen the development of finite element crystal plasticity[11,12] models. In all cases, a large number of fitting parameters are necessary to characterize the yielding and hardening of the different slip and twinning modes and their interactions during deformation. In order to fit these models, experiments are conducted (usually uniaxial tension and compression) often on strongly textured materials to try to isolate particular deformation mechanisms.[13] Understanding and modeling of deformation in strongly textured materials is often easier than for the case of weak textures. For example, one can use a combination of experimental tests which includes through-thickness compression, in-plane tension, and in-plane compression on a materials with a typical basal sheet texture to fit the deformation parameters, for basal and second-order pyramidal $\langle c+a \rangle$ slip, basal + prism

P. TOMLINSON, Doctoral Candidate, H. AZIZI-ALIZAMINI, Research Associate, W.J. POOLE, Professor, and C.W. SINCLAIR, Associate Professor, are with the Department of Materials Engineering, The University of British Columbia, Vancouver, BC, V6T 1Z4, Canada. Contact e-mail: warren.poole@ubc.ca M.A. GHARGHOURI, Senior Research Officer, is with the Canadian Neutron Beam Centre, Chalk River, ON.



Manuscript submitted September 4, 2012.
Article published online March 28, 2013

slip and extension twinning, respectively,[9,14] *i.e.*, these models can be successfully applied to situations where deformation is dominated by either slip or by twinning. However, as recently pointed out by Agnew,[2] these models face challenges when combinations of slip and twinning are found. This is the situation in weaker-textured materials and also situations when complex stress states are present.

Multiaxial deformation of magnesium is important from a number of perspectives including complex forming of magnesium parts and in-service performance, *e.g.*, automotive applications.[15] A number of studies have examined strain paths other than uniaxial tension or compression, *e.g.*, ring hoop tension[16] or simple shear.[17] The forming of magnesium has been examined using forming limit diagrams[18–20] and through simplified forming tests such as deep drawing[21] and bending[22] (including spring back[23,24]). Further, testing relevant to crash performance of a potential magnesium-intensive front end has been conducted by tests of bending and crushing of magnesium tubes.[25] From a more fundamental perspective, there have been a limited number of attempts to characterize yield loci using, for example, cruciform samples[26] or a variety of sample orientations and geometries.[27] From a modeling point of view, phenomenological descriptions of yield surface[28–31] and the evolution of yield surface with plastic strain[31–33] have been developed. However, there is a lack of high-quality experimental data for multiaxial deformation behavior. It is this lack of data, which provides one of the motivations for the current study. Continuous stress–strain curves have been measured to evaluate the effect of stress state on the initiation and evolution of plastic deformation using thin-walled tubes loaded under a combination of axial tension/compression and internal pressure. Further, the study assesses the predictive capability of VPSC which has previously been fit to a comprehensive set of tension/compression tests for AZ80 with different textures.[9] Finally, the evolution of crystallographic texture will systematically evaluated for a range of biaxial loading conditions.

## II. METHODOLOGY

The material used in this study was the magnesium alloy AZ80 (Mg-8wt pct Al-0.5wt pct Zn). Two sources of material were examined, *i.e.*, (a) an as-cast direct chill alloy, and (b) extruded bar 30 mm in diameter. All samples were heat treated at 688 K (415 °C) for 24 hours and then water quenched before machining the samples to produce a supersaturated solid solution containing no $\beta$ $Mg_{17}Al_{12}$ phase. Samples for uniaxial compression tests and tensile tubes were machined from a solid extruded bar. Tubes were fabricated by first drilling a hole through the solid bar, then mounting the specimen on a mandrel and machining the outer dimensions in a lathe. This ensured a consistent wall thickness over the gauge section. After machining, the samples were annealed for 1 hour at 658 K (385 °C) to remove any surface deformation. The average initial grain size was determined from optical micrographs using ASTM E112, and the initial texture was measured at the Canadian Neutron Beam Centre using the E3 spectrometer (data for $\{0001\}$, $\{10\bar{1}0\}$, $\{10\bar{1}1\}$ and $\{10\bar{1}2\}$ pole figures were collected). The orientation distribution function (ODF) was calculated using the MTEX open source software.[34] All experimental pole figures shown in the current article were recalculated from the experimentally determined ODF.

The microstructure of the cast material, shown in Figure 1(a), was found to have an average grain size of 32 $\mu$m. The crystallographic texture was observed to be relatively weak but not completely random (see Figure 7 in Section III, the maximum intensity was 1.8× random). This presumably is related to some preferred orientation of growth during solidification.[35] A small number of insoluble Mn-rich particles (1 through 5 $\mu$m in diameter) could be observed in the optical micrographs, but it was assumed that the relatively large size and very low volume fraction of these particles would not influence the macroscopic yield stress and work hardening behavior. The extruded AZ80 had a slightly smaller grain size of 20 $\mu$m, and some stringer-type inclusions could be observed in the optical microscope, see Figure 1(b) and also Reference 36. The crystallographic texture of the extruded material was also relatively weak although stronger than the as-cast material, *i.e.*, maximum intensity of 2.3× random *vs* 1.8× random. In this case, the [0001] poles also tended to be oriented away in a band around the TD–RD plane (a pole figure of the initial texture for the extruded material is shown as an inset in Figure 10). The results presented in the article primarily arise from cast material. At the end of the article, results are presented to demonstrate the important effect of the initial texture.

The mechanical response of the material was measured using hollow tubular samples similar to those used by Marin *et al.*[37] (see Figure 2(a)). The dimensions of the reduced section were a gauge length of 50 mm, an outer diameter of 18 mm, and a wall thickness 0.9 mm. For cast and extruded materials, the axial tensile/compression direction was parallel to the casting direction or parallel to the extrusion direction, respectively.

Tests on the tubular samples were conducted in an Instron 8874 servohydraulic load frame. Biaxial tests were conducted by using a combination of applied tensile or compression force and internal pressure as shown schematically in Figure 2(b). The samples were internally pressurized with hydraulic oil which was compressed using a SITEC pressure generator (*i.e.*, a piston that compresses the hydraulic fluid). The maximum pressure that this system can generate is 200 MPa which for the current geometry corresponds to a maximum hoop stress of ≈2000 MPa. The sample geometry chosen has a radius to thickness ratio of ≈10:1 which falls in the range where thin-walled pressure vessel equations can be used.[38] As such, the axial and hoop stress at any point can be calculated as:

$$\sigma_{\text{axial}} = \frac{F}{A} + \frac{Pr}{2t} \quad [1]$$

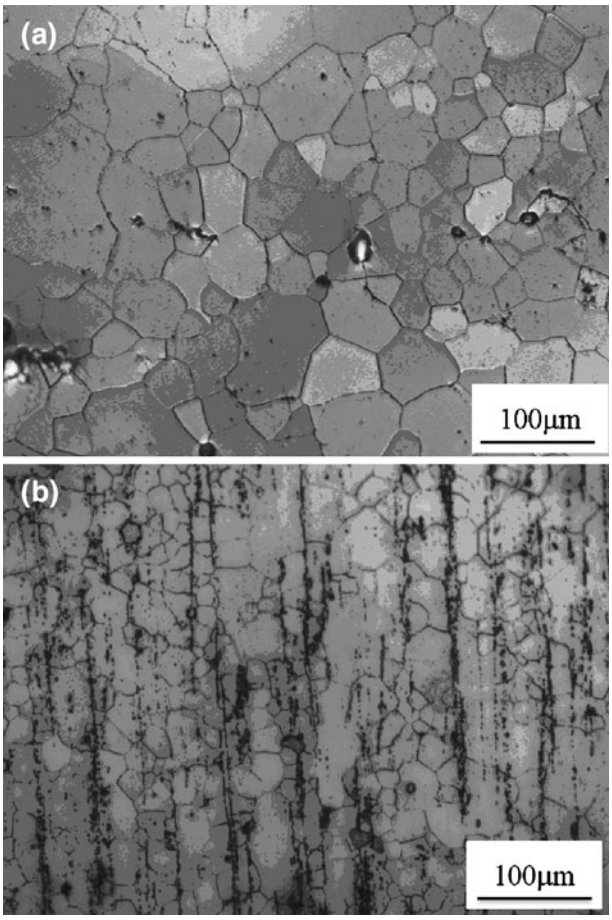


Fig. 1—Optical micrographs of microstructure for (*a*) cast and (*b*) extruded AZ80 (after heat treatments).

where $F$ is the force measured from the load cell and $A$ is the instantaneous area and

$$\sigma_{\text{hoop}} = \frac{Pr}{t} \quad [2]$$

where $P$ is the measured internal pressure, $t$ is the instantaneous thickness and $r$ is the average instantaneous radius, *i.e.*, $(r_{\text{inner}} + r_{\text{outer}})/2$.

$$\sigma_{\text{radial}} = 0 \quad [3]$$

During the test, the ratio of axial-to-hoop stress was maintained nearly constant (within 5 pct) by controlling the internal pressure with respect to the applied axial load. This was done using a LabView program with a virtual PID controller, *i.e.*, the control point for the pressure generator was continuously updated based on the current axial load measurements from the load cell. For the case of uniaxial tension or compression on tubular samples, no hydraulic fluid was introduced into the sample, *i.e.*, the internal pressure was zero. Tests were conducted on the as-cast and extruded materials for nominal biaxiality ratios (defined as $\frac{\sigma_{\text{hoop}}}{\sigma_{\text{axial}}}$) of $0_{\text{tension}}$, 0.5, 1.0, $\infty$, $-0.5$ and $0_{\text{compression}}$ (note, in the current study the hoop stress can only be positive and that

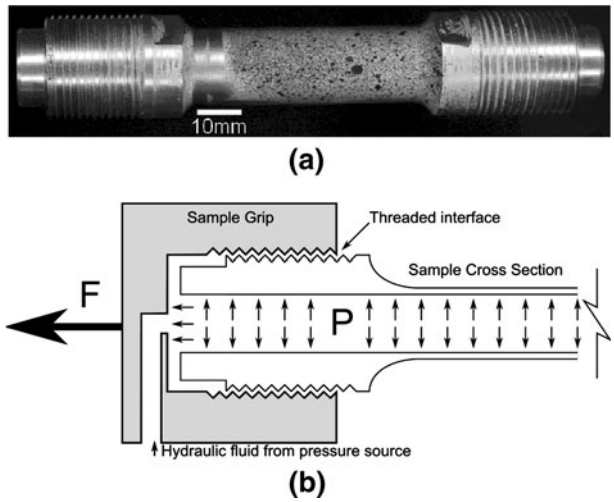


Fig. 2—Sample design for biaxial tests: (*a*) optical macrograph of test specimen and (*b*) schematic diagram illustrating the gripping of the sample and the axial force and internal pressure.

uniaxial tension or compression both have biaxiality ratios of 0 and so they are hereafter referred to as axial tension or compression, respectively).

The axial displacement in the gauge length of the sample was measured during the test with a clip on extensometer with a gauge length of 25 mm. Axial and hoop displacements were also simultaneously measured using the LaVision digital image correlation (DIC) system, the resulting displacements being post-processed to obtain the average true strain in the gauge section of the sample.[39,40] Before testing, the sample was painted white with an enamel spray paint followed by a light dusting with black enamel spray paint to produce the speckle pattern as seen in Figure 2(a). For each test, a comparison was conducted between the results for axial strain from the extensometer and the DIC system to verify the DIC measurements. All the results reported later in the current article come from the DIC analysis. In order to check for consistency of all tests, the initial elastic modulus was compared with the expected value using Generalized Hooke's Law with a Young's modulus of 45 GPa and a Poisson ratio of 0.3. Magnesium is nearly elastically isotropic[41] so that small variations in texture were assumed to have a negligible effect on these calculations.[41] In all the cases reported, the agreement was within 5 pct.

As the current study is primarily concerned with the plastic response, the data were analyzed to remove elastic strains and to correct for dimensional changes during the test so that true stress and true plastic strain can be reported. The elastic strains for the axial and hoop strain were calculated using Generalized Hooke's Law and then subtracted from the measured strain. Using the data from the image correlation system, the axial and hoop plastic strains could then be calculated. The radial plastic strain was then determined assuming constancy of volume during plastic deformation, *i.e.*,

$$\varepsilon_{\text{radial}} = -\left(\varepsilon_{\text{axial}} + \varepsilon_{\text{hoop}}\right) \quad [4]$$

This allowed for continuous true stress–true plastic strain curves to be determined for the various biaxaility ratios. Using these data, the results from various loading paths could be examined in either stress or strain space. In the case of the data in strain space, the derivative of the hoop strain *vs* axial strain was calculated to characterize the evolution in strain ratio as a function of deformation. To this end, an *n*th order polynomial (between third and eighth order depending on the dataset) was fit to the experimental data to get hoop strain as a function of axial strain. This polynominal was then analytically differentiated to provide a smooth derivative.

The tubular samples were tested until either fracture or buckling occurred. Fracture was observed to coincide with the load or pressure dropping to zero. Plastic buckling was determined by optical observation. After the test, a 10-mm-wide annular ring was cut from the gauge length away from the fracture surface. This annular ring was further sectioned parallel to the tensile axis into eight pieces which were stacked to produce a sample suitable for neutron diffraction measurements, *i.e.*, a volume of $\approx$1000 mm$^3$. The texture measurements were conducted and analyzed in a similar manner to that described earlier for the starting materials.

Polycrystal plasticity simulations were made using a modified version of the VPSC code of Lebensohn and Tomé.[8] The VPSC 7 code was modified to allow the simulations to mimic as closely as possible the conditions imposed experimentally. For all cases, mixed boundary conditions were imposed. Deformation was imposed parallel to the axis of the sample, and all macroscopic shear strains were imposed to be zero. The stress normal to the sample wall was also imposed to be zero. To obtain simulations with fixed stress biaxiality, the hoop stress was controlled based on the value of the axial stress. This required that an additional iterative step be performed at each step of the imposed axial deformation to determine the appropriate value for the hoop stress. Starting with the axial stress from the previous deformation step as an initial guess, the hoop stress was calculated from the target biaxiality and the simulation step performed to obtain the corresponding axial stress. The resulting biaxiality was then calculated and compared with the target biaxiality. Based on the difference between the calculated and target biaxialities and using a bisection scheme, the hoop stress was modified, and the deformation step repeated until the difference between the calculated and target biaxiality was less than 1 pct. Once this condition was reached, the slip system and twin system information was updated (*i.e.*, their hardening and any change in the twin fraction), the texture updated, and the deformation continued to the next level of imposed axial strain. This procedure was suitable for simulating biaxialities between 0 and 2, consistent with those explored experimentally, but was not suitable for obtaining data for higher biaxialities. For biaxialities greater than 2, the deformation is dominated by imposing the stress in the hoop direction and thus calculations controlled by an imposed axial deformation failed to converge. The experimentally determined orientation distribution function of the initial material was used to create a set of 16,416 weighted discrete orientations, the 15,000 orientations with the highest intensity being used for input to VPSC. In order to test the predictive capabilities of the model, the model input parameters (critically resolved shear stresses, hardening parameters, rate sensitivity, grain interaction stiffness, *etc.*) were identical to the ones used by Jain *et al.*[9] recently reported for AZ80.

The VPSC simulations were conducted for a wide range of biaxiality ratios so as to create a locus of points at (a) the onset of plasticity, (b) equivalent plastic work corresponding to an equivalent tensile deformation of 0.005 and 0.03 (note: this will be discussed further in Section III). In addition, the incremental shear strain on each slip system in each grain was monitored during simulations. This information has been extracted after one step of simulated deformation (corresponding to an axial strain of 0.01) and represented using two stereographic {0001} pole figures. The starting grain orientations (which represented all possible orientations) were plotted on the {0001} pole figure, and binned into 2 deg $\times$ 2 deg regions. One pole figure was constructed to show the slip/twin system that was most active (had the highest incremental shear strain) during the first step of deformation. The second pole figure was constructed to show the magnitude of this shear strain on the most active system.

## III. RESULTS

Figure 3 illustrates examples of experimental results for the true stress–true plastic strain response of the cast AZ80 under a various loading conditions. Figure 3(a) compares the results for the uniaxial tests on the tubular samples, *i.e.*, axial tension, hoop tension and axial compression. In all cases, a high rate of initial work hardening is observed but decreases to a much lower level by a plastic strain of 0.01. For the tension tests, the end point of the curve represents the onset of localization after which failure was rapidly observed. In the case of compression, the data are plotted up to the onset of observable plastic buckling. It can be observed that the stress–strain curves for compression and hoop tension are similar while the flow stress for axial tension is $\approx$60 MPa higher. The presence of serrations in the stress–strain curves has been observed previously by Corby *et al.*[42] for a similar alloy (AZ91) and is related to the complex dynamic interplay between solutes (Al and Zn) and mobile dislocations. Figures 3(b) through (d) show the results for tests done at various biaxiality ratios, ($\frac{\sigma_{\text{hoop}}}{\sigma_{\text{axial}}}$), *i.e.*, 0.4 and 0.9, and $-0.5$. In these cases, there are two stress–strain curves for each test: one for axial stress *vs* axial plastic strain, and one for hoop stress *vs* hoop plastic strain. Here, it is worth emphasizing that at a given plastic axial strain, one cannot directly observe the corresponding plastic hoop strain on this type of plot except for the end point of both curves which are both at the same level of overall deformation. However, with this in mind, one can make several general observations: (a) the stress–strain behavior in the axial direction occurs at higher stresses than for the

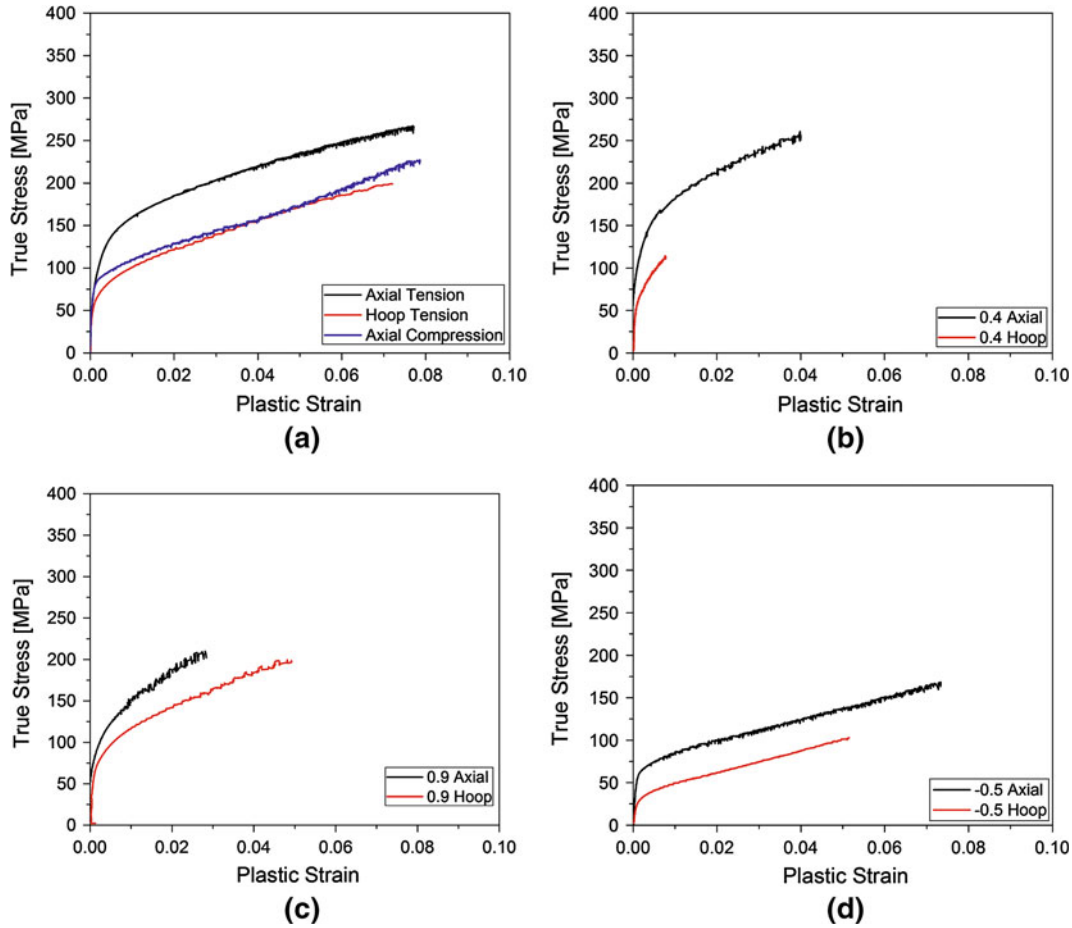


Fig. 3—Experimental true stress *vs* true plastic strain curves for the cast AZ80, (*a*) uniaxial tension, hoop tension, and axial compression; (*b*) biaxiality stress ratio 0.4; (*c*) biaxiality stress ratio 0.9; and (*d*) biaxiality stress ratio −0.5. Note: axial stress is parallel to cast direction and hoop stress is perpendicular to cast direction.

hoop direction, (b) the magnitude of hoop strain increases as the biaxiality ratio increases, and (c) in the case of a biaxiality ratio of 0.9, the hoop strain is 1.7 times the axial strain even though the hoop stress is actually slight lower than the axial stress.

The data from the biaxial tests have been used to generate the surfaces of the plastic potential in stress state at two levels of imposed deformation. For multiaxial loading of an anisotropic material such as the magnesium in this study, the definition of equivalent deformation levels is nontrivial. In the current study, we have chosen to define the equivalent deformation in terms of equal levels of external plastic work done as an operational definition to compare the plastic potentials from the experiments and simulations. For a complex, loading path, the work done per unit volume can be calculated by integrating:

$$W = \int_{o}^{\varepsilon} \sigma_{ij} d\varepsilon_{ij}^{p}$$

where $\sigma_{ij}$ is the true stress and $\varepsilon_{ij}^{p}$ is the true plastic strain.[43] In the current case, the work done is calculated from the stress–strain response in the hoop and axial directions. We have chosen two levels of plastic work, 0.5 and 4.6 MJ/m$^3$, which correspond to a plastic strain of 0.005 and 0.03 in uniaxial tension parallel to the cast direction. This corresponds to a plastic strain after yielding and a strain at which the flow stress has approximately doubled due to work hardening.

Figure 4 presents the experimental and VPSC results for different loading paths in stress space at equal levels of plastic work. Note, the solid circular symbol for compression parallel to the hoop direction is taken from the previous study of Jain *et al.*[44] on the same material. A short red line has been added through each of the experimental axial/hoop stress data points. The slope of this line represents an orthogonal vector to the experimentally determined strain vector at this level of plastic work, *i.e.*, this follows from the principal of normality and represents the slope of the plastic potential.[43] The VPSC predictions are plotted as a combination of solid and dashed lines for each level of plastic work. The solid line represents the simulation results while the dashed lines are interpolations through the regions of stress space where predictions were not made. Simulations were conducted for uniaxial tension and compression parallel to the TD direction and these were used in the interpolation.

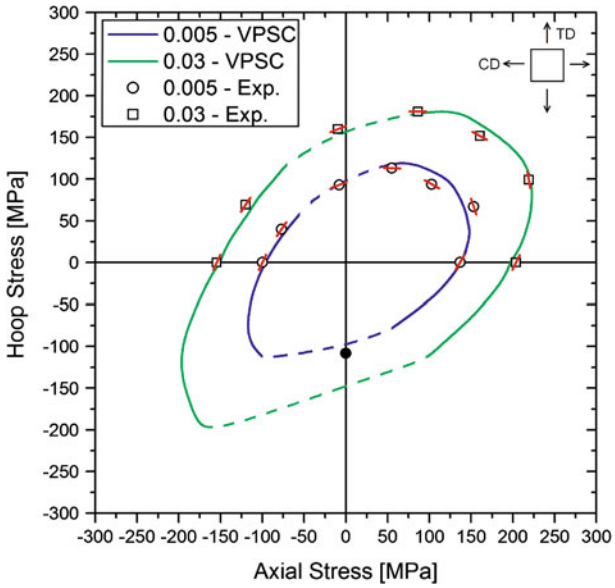


Fig. 4—Plastic potential of the cast AZ80 for different levels of plastic deformation. The circular symbols and the blue line represent an equivalent plastic work of 0.5 MJ/m$^3$ and the square symbols represent an equivalent plastic work of 4.6 MJ/m$^3$. These levels of plastic work correspond to tensile strains in the axial direction of 0.005 and 0.03, respectively. The solid circular symbol for compression in the TD direction is from uniaxial compression tests the study of Jain *et al.*[43] on the same material. Note: axial stress is parallel to cast direction (CD) and hoop stress is perpendicular to CD.

A number of observations can be made from these results: (a) one can see that the agreement between the experimental and VPSC results for the stress surfaces at both levels of plastic work are within ±10 pct and (b) the experimentally determined strain response (represented by the red lines perpendicular to the strain vectors in the figure) and the tangents of the VPSC flow surface are in good qualitative agreement. Further, one can observe that the material response is relatively anisotropic. The experimentally determined tension/compression asymmetry for loading in the CD is 1.4 at low strains and 1.3 at the higher level of plastic strain while the for loading in the TD direction is 0.9 and 0.75, respectively (as previously reported for this material[9]). Second, the results qualitatively show that there is relatively little evolution in the tangent to the plastic potential with increasing strain with the exception of the biaxiality ratio of 0.4 where it appears that there is a significant change in the tangent when the plastic strain increases.

To examine the evolution in the biaxial strain response for different biaxial stress states, it is also useful to plot the experimental results in strain space. Figure 5 shows the results from the current study plotted in this manner. In general, this confirms that there is relatively little evolution in the ratio of hoop strain to axial strain, except for the case of a biaxial stress ratio of 0.4 where both the experiments and VPSC simulations show a significant evolution. To examine this in more detail, a polynominal function was fit to the curves and then analytically differentiated as described in Section II. Figure 6 shows the results of this analysis

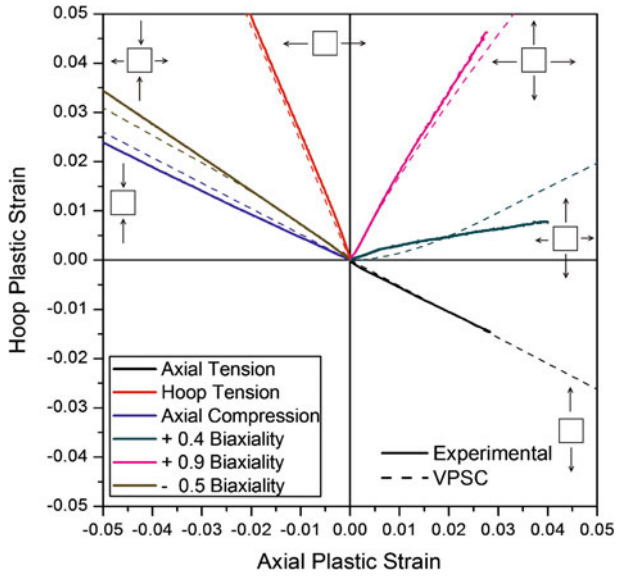


Fig. 5—Experimental and VPSC results plotted in hoop strain/axial strain space for the various biaxiality ratios.

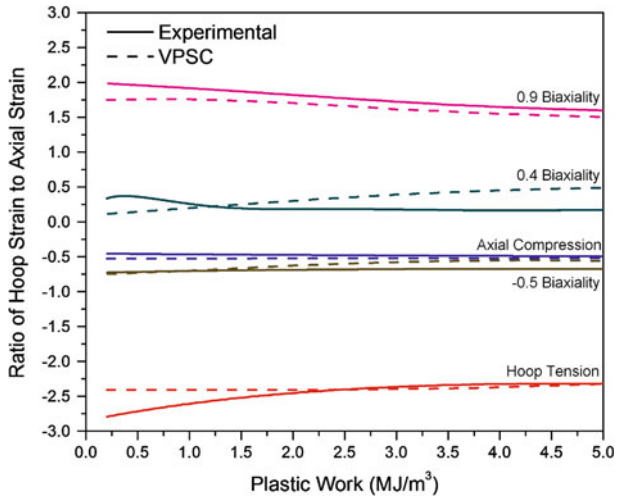


Fig. 6—Experimental and VPSC results for the evolution of the hoop-to-axial strain ratio as a function of the applied plastic work. For reference, a plastic work of 5 MJ/m$^3$ corresponds to an equivalent axial tensile strain of approximately 0.03.

where the derivative, $\frac{d\varepsilon^p_{\text{hoop}}}{d\varepsilon^p_{\text{axial}}}$, is plotted as a function of plastic work. Here it can be observed that for axial compression, the strain ratio is nearly constant as a function of plastic work and has a ratio of ≈0.5, similar to the expected value for an isotropic material (note that a similar result was found for axial tension but is not shown here as it overlaps with compression curve). For the case of a biaxiality ratio of 0.4, the experimentally determined strain ratio starts at 0.2 and decreases to a value of 0.1 and then remains almost constant. In contrast, the VPSC simulation has an initial strain ratio of 0.1 and the increases to value of 0.5. For a biaxiality of 0.9, the experimental and VPSC ratios starts at 1.75 to 2.0 and then slowly decrease in linear manner to 1.5 at

plastic work 5 MJ/m$^3$ (note: for an isotropic von Mises material at a biaxiality ratio of 1, the strain ratio is 1, this illustrates the large degree of anisotropy in this material which has a relatively weak texture). In the case of hoop tension, the experimental strain ratio starts at −2.75 and gradually increases to a value of −2.4 near the end of the test which compares to an expected value of −2 for an isotropic material.

The evolution of crystallographic texture can be observed by comparing equal area pole figures measured for the initial material and samples after fracture or buckling point. Table I summarizes the axial and hoop plastic strains for which the texture measurements and the VPSC simulations were conducted. Figure 7(a) is the {0001} pole figure determined from the neutron diffraction measurements while Figure 7(b) illustrates the input texture for the VPSC simulations. Figure 7(a) shows that the starting texture of the cast material is quite weak (maximum of 1.8× random) but there is a preferred orientation of grains which form a relatively wide band about the orthogonal direction to the casting direction, *i.e.*, there are almost no grains with {0001} parallel to the casting direction. One can observe that the input texture shown in Figure 7(b) is a good representation of the initial texture. Figure 8 summarizes the pole figures at different biaxiality ratios for the strains summarized in Table I. From left to right, one observes (a) the experimentally determined texture, (b) VPSC simulations for texture, (c) the VPSC predictions for the orientation dependent slip system with the highest activity and (d) the VPSC orientation dependence of the magnitude of strain increment at an imposed far field strain of 0.01. The latter two pole figures will be helpful for rationalizing the texture evolution for different biaxiality ratios in the discussion of Section IV.

**Table I. Summary of the Axial and Hoop Plastic Strains for Which Crystallographic Texture Measurements and VPSC Simulations Were Conducted, *i.e.*, the data in Fig. 8**

| Stress-state | Axial Plastic Strain | Hoop Plastic Strain |
|---|---|---|
| Axial Tension | 0.08 | −0.04 |
| Hoop Tension | −0.03 | 0.07 |
| 0.4 | 0.04 | 0.01 |
| 0.9 | 0.03 | 0.05 |
| −0.5 | −0.08 | 0.05 |
| Axial Compression | −0.08 | 0.04 |

Note: axial strains are parallel to the casting direction (CD) and hoop strains are perpendicular to the casting direction.

The crystallographic texture after uniaxial tensile deformation can be observed in Figure 8(a). In comparison with the initial texture in Figure 7(a), it can be observed that the overall nature of the texture has not changed but there has been significant strengthening of the initial texture with the maximum intensity now at 2.7× random and the width of the band about the TD–ND plane narrowing. In addition, one can observe that there is some variation of the texture as function of angle that the [0001] poles make around the CD direction, *i.e.*, the intensity of the band in the TD–ND plane is not uniform. The VPSC predictions are in good qualitative agreement with the experimental measurements: however, the intensity of the texture is stronger.

For the case of a biaxiality ratio of 0.4 shown in Figure 8(b), one can observe that the maximum intensity of the texture component near the center of the pole figure has increased to 3.2× random compared with ≈1.5× random in the initial texture. Further, it can be seen that there is a significant reduction in the intensity at the rim of the pole figure. Again, the results from the VPSC simulations are in qualitative agreement although predicting a somewhat stronger texture strengthening. Figure 8(c) illustrates the results for a biaxiality ratio of 0.9 where it can be clearly observed that the intensity at the center of the pole figure has dramatically increased to 4.2× random experimentally and 5.2× random for the VPSC simulations. Again the increase in intensity at the center of the pole figure is accompanied by a decrease at the rim of the pole figure. Figure 8(d)

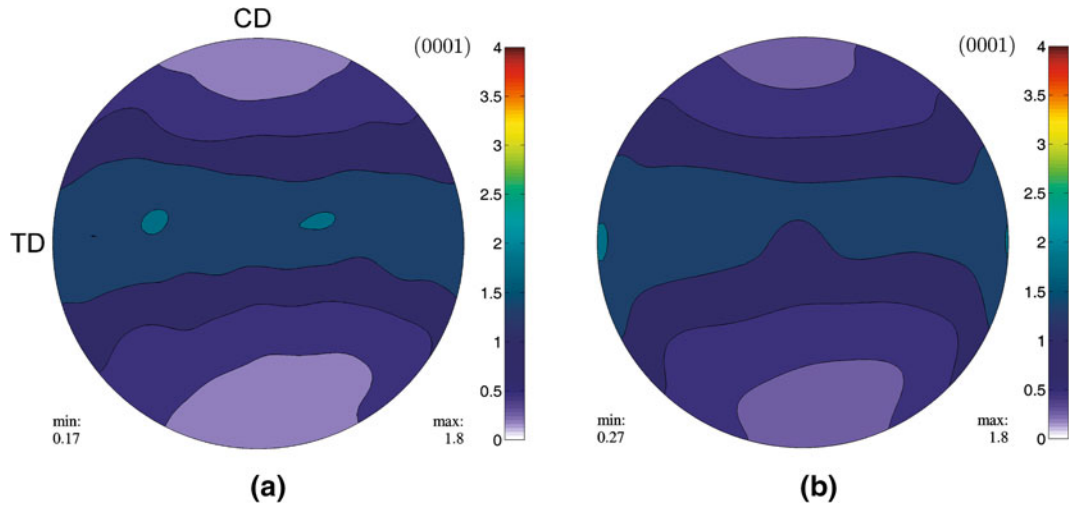


Fig. 7—(0001) equal area pole figures illustrating the initial texture, (*a*) experimentally determined (reconstructed from the ODF), (*b*) the input texture used for VPSC.

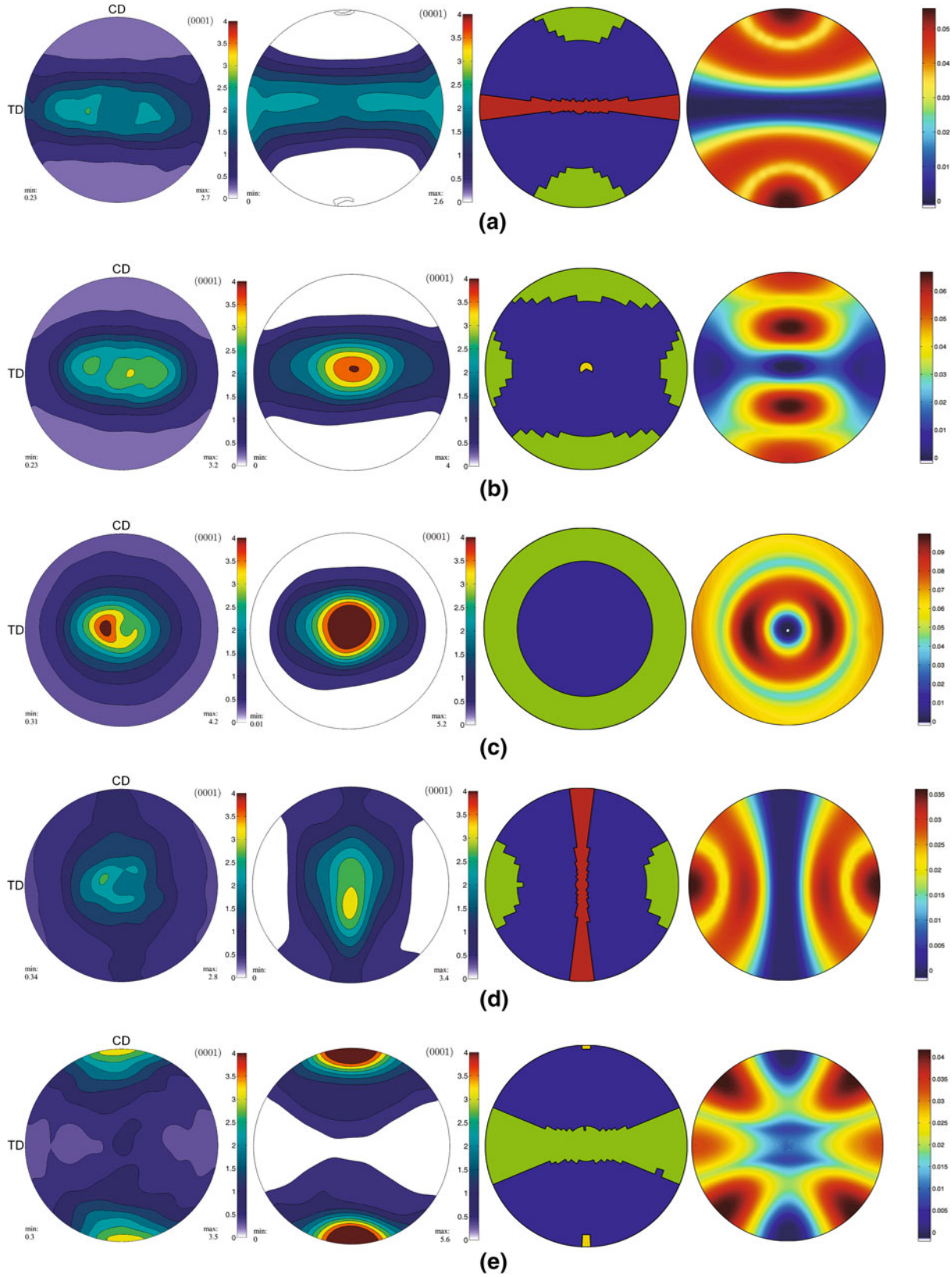


Fig. 8—Pole figures describing results for different biaxiality ratios: (*a*) uniaxial tension, (*b*) 0.4, (*c*) 0.9, (*d*) hoop tension, (*e*) −0.5, and (*f*) axial compression. For each stress state, (0001) pole figures which represent from left to right: (*i*) experimental pole figures at the end of the test (axial and hoop strains are summarized in Table I); (*ii*) VPSC simulation predictions for the same combination of axial and hoop strain; (*iii*) orientation dependence of the most active deformation system predicted by VPSC. Colors correspond to the most active slip/twin system: Blue = Basal slip, Red = Prism Slip, Yellow = second-order Pyramidal Slip, Green = Extension Twinning); and (*iv*) the orientation dependence of strain on the most favored system. The color scale on the right corresponds to the strain increment in the first step of deformation at an imposed far field strain of 0.01. Note: Axial stress/strain are parallel to CD and hoop stress/strain are parallel to TD.

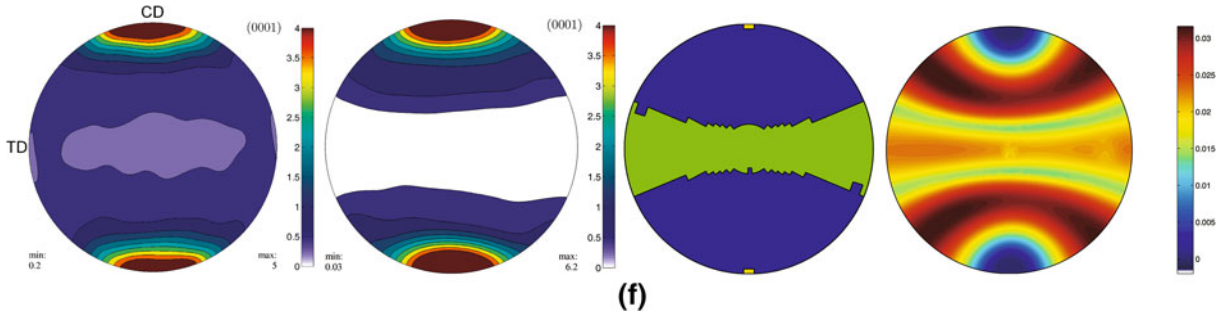


Fig. 8—continued.

presents the results for hoop tension (*i.e.*, tension perpendicular to the results in Figure 8(a)). In this case, the experimental and VPSC results now show that a band of preferred orientations is found in the CD–TD plane with a peak at the center of the pole figure. Turning to the compression-tension quadrant of stress space, one observes a dramatically different evolution of texture. For a biaxiality ratio of −0.5 shown in Figure 8(e), one now sees a significant increase in intensity of poles parallel to the CD direction and a weakening of poles perpendicular to CD from both the experiments and VPSC simulations. Finally, Figure 8(f) presents the results for compression parallel to the CD direction. Here, the experimentally determined intensity of poles parallel to CD has increased from ≈0.25× random (see Figure 7(a)) to 3.5× random and the intensity along perpendicular to the CD direction has decreased from 1.5 to 1.7× random to 0.25 to 0.5× random. The VPSC texture simulations shown in Figures 8(e) and (f) are again in qualitative agreement with the experimental values but with somewhat sharper textures.

Figures 9(a) through (d) present the predictions from VPSC for the evolution of overall activity on the basal ⟨a⟩, the prism ⟨a⟩, second-order pyramidal ⟨c + a⟩ and $\{10\bar{1}2\}$extension twin system for the different biaxiality conditions, and Figure 9(e) presents the evolution of extension twin volume fraction. The results can be summarized as follows: (a) for all cases, basal slip comprises from 55 to 85 pct of the activity; (b) extension twin activity increases as the hoop stress increases and the axial stress changes from tension to compression (there is a commiserate decrease in basal activity); (c) prism activity is initially very low, but for axial tension and biaxiality ratio of 0.4 and 0.9, the activity increases from 10 to 25 pct of total activity as the level of plastic work increases (note: a plastic work value of 10 corresponds to equivalent axial tensile strain of 0.055); and (d) the activity of pyramidal slip is predicted to be almost zero for all cases examined.

## IV. DISCUSSION

The deformation response of the cast AZ80 is clearly complex and involves the interplay between the preferred orientation of grains, the applied stress state, and the activity levels of the various underlying deformation modes. In this section, the relationship between the macroscopic stress and strain response will be rationalized taking these factors into account. First, it is worth making some general observations regarding the basic deformation mechanisms that occur in this material. A previous study on this same material by Jain *et al.*[45] used slip trace analysis after a compressive pre-strain of 0.05 to show that there was experimental evidence that a combination of basal ⟨a⟩, prism ⟨a⟩, and second-order pyramidal ⟨c + a⟩ slip operate at this level of strain although it was not possible to quantify their relative activity levels. It was also shown that in most cases, the slip activity occurred on the systems with the highest Schmid factor. Further, extension twins were common, sometimes even consuming entire grains.[45] A very limited number of fine contraction twins were also observed[9] and thus, it will be assumed that owing to the low volume fraction of contractions twins experimentally observed, the effects of these on the macroscopic behavior can safely be ignored. The VPSC simulations predict that the predominant deformation mechanisms at the beginning of plastic deformation in the weakly textured material was basal ⟨a⟩ slip and extension twinning $\{10\bar{1}2\}$, which is consistent with the general observation that, at room temperature, these deformation modes have the lowest critically resolved shear stress.[13,14]

### A. *Macroscopic Stress and Strain Response*

The shape of plastic potential and the presence of a significant tension/compression asymmetry demonstrates that even though the texture is quite weak, there remains a significant asymmetry of the plastic work surface, this arising from the intrinsic sensitivity of twinning to sense of the loading in individual grains. As mentioned earlier, even though this material has a cast texture, one can view it as a weak version of a typical extrusion texture where the majority of grains are oriented in a band perpendicular to the extrusion direction or in this case the casting direction (see[46] for example of a typical extrusion texture in AZ31B). The role of this type of texture on yielding has been discussed in detail by Barnett.[3,27] The main effect arises from the fact that while extension twinning is an easy deformation mechanism to activate, one must consider

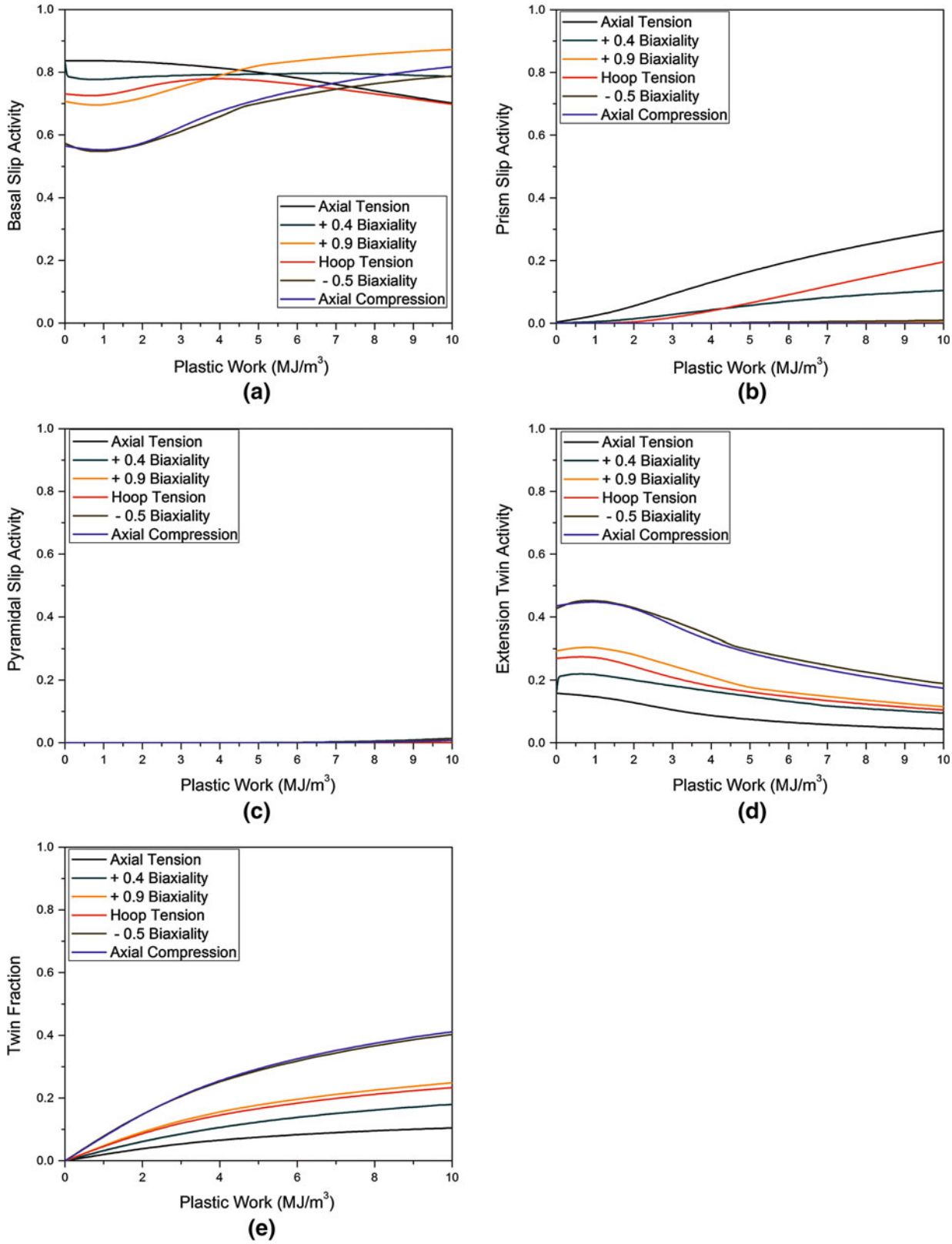


Fig. 9—VPSC predictions of slip and twin activities/volume fraction as function of applied plastic work, (*a*) basal ⟨a⟩, (*b*) prism ⟨a⟩, (*c*) second-order pyramidal ⟨c + a⟩, (*d*) $\{10\bar{1}2\}$ extension twins activity and (*e*) $\{10\bar{1}2\}$ extension twins volume fraction. Note: a plastic work of 10 is approximately a uniaxial tensile strain in cast direction of 5.4 pct.

its polar nature, and its ability to accommodate the applied strain. For the present results, the effect of stress state is well illustrated by the VPSC predictions for the orientation dependence of the most active slip system and increment of strain associated with this system shown in Figure 8. It is useful to first consider the case of uniaxial tension parallel to the cast direction and then examine how changing the stress state impacts the situation. In the case of uniaxial tension parallel to the cast direction, VPSC predicts that grains oriented with basal poles parallel to CD show high activity of extension twinning and a large shear strain increment associated with this (see Figure 8(a)). However, referring back to the initial texture shown in Figure 7(a), it can be seen that grains in this orientation correspond to the region of orientation space where there is a low probability of grains being present. On the other hand, grains oriented perpendicular to CD are well aligned for prism slip, but the stress to activate this system is much higher than basal slip, and as a result, the strain increment in these grains is low. The overall deformation behavior shown in Figure 9 indicates that deformation is initially attributed to basal slip (≈85 pct) with some extension twinning. As deformation proceeds and the resolved shear stresses increase, prism slip starts to activate and by a strain of 0.05 approximately, 25 pct of the activity can be attributed to this mechanism. This scenario leads to the high overall macroscopic stress for deformation to occur.

As the hoop stress is now increased to 0.4 of the axial stress, the situation changes. An examination of Figure 8b shows that the most active deformation mechanisms are basal slip and extension twins. There is a very small region at the center of the pole figure where the grains are oriented such that second-order pyramidal is predicted to operate, but this represents few grains which can safely be ignored. The region of grains oriented for extension twinning is expanded near CD and a new region appears near TD. However, again there are few grains in the former orientation, and the grains in the latter orientation show a very low level of shear strain increment. As such, Figure 9 shows predictions very similar to axial tension, *i.e.*, at the onset of plasticity, 80 pct basal with prism slip increasing to approximately 10 pct at the a plastic work of 10 $MJ/m^3$ (for reference approximately a strain of 0.055 in uniaxial tension).

When the biaxiality ratio increases further such that the hoop stress-to-axial stress ratio is 0.9, the situation evolves further. In Figure 8(c), it can be observed that all grains oriented at rim of the pole figure predominantly deform by extension twinning, there is a high level of strain increment associated with these grains, and there is significant volume fraction of grains in this orientation space (see Figure 7(a)). As such, the overall twinning activity at the onset of deformation increases to ≈30 pct of the activity, and basal drops to ≈70 pct. With increasing strain or plastic work, these now remain the only deformation mechanisms as shown in Figure 9, *i.e.*, prism slip is now suppressed. These biaxiality conditions (*i.e.*, 0.4 and 0.9) represent cases where there is a very close competition between basal, prism, and extension twinning. This range of stress states corresponds to the "corner" of the plastic potential where the orientation of normality condition is rapidly evolving. As such, these represent difficult conditions to simulate, and it is the region where the poorest agreement is found between the plastic potential predicted by VPSC and the experiments. Further, at a biaxiality ratio of 0.4, VPSC has the poorest performance in predicting the ratio of hoop to axial strain and its evolution as shown in Figures 5 and 6.

As we now move to the stress state of hoop tension, the situation again changes significantly as shown in Figure 8(d). The slip system with the highest activity and the strain increment pole figures are similar to the case of axial tension shown in Figure 8(a) but are now rotated by 90 deg about ND. However, there is an important difference between the two cases. Now, the orientations where extension twinning is active corresponds to a region in the initial texture (Figure 7(a)) where there is a higher than random probability of finding grains. The VPSC simulations predict that initially the situation is similar to the biaxiality ratio of 0.9, *i.e.*, ≈70 pct basal slip and ≈30 pct extension twinning (Figures 9(a) and (c)). However, in this case, it is predicted that prism slip will be activated as deformation proceeds (Figure 9(b)).

Turning now to the compressive quadrant of stress space (a biaxiality of −0.5 and axial compression), it can be seen that a situation arises where extension twinning is favored. From Figures 8(e) and (f), it can be observed that the band of grains oriented at 90 deg to CD has high activity of extension twinning, and this corresponds to the region in the initial texture where there is a much higher than random probability of finding grains (Figure 7(a)). As such, for both these scenarios, the overall activity of extension twinning is maximum (≈45 pct of activity) at a low level of plastic strain, and the total volume fraction of material that is predicted to undergo extension twinning is predicted to be 40 pct after a plastic work of 10 $MJ/m^3$ (recall, this is an equivalent axial tensile strain of 0.055). The activity of extension twinning decreases as the level of deformation increases since the probability of finding grains in the orientation space favorable to twinning decreases. The one difference between a biaxiality ratio of −0.5 and axial compression is the low strain increment associated with grains oriented at the center of the pole figure (both for extension twining and basal slip).

The preceding section has attempted to rationalize in detail how the deformation behavior at the grain level evolves with the imposed stress state. It is worth summarizing some general comments about the overall macroscopic effects. First, as discussed earlier, extension twinning is a relatively easy deformation mode to operate compared with prism or pyramidal slip so that when it is favorable, deformation at the macroscopic level is easier. Thus, the tension/compression asymmetry for loading in the CD can be understood as a combination of the high amount of extension twinning in axial compression and the high stress required to activate prism slip in axial tension. Further, the tension/compression asymmetry at low plastic strains for loading

perpendicular to the cast direction is low, and the value of the flow stress is similar to axial compression parallel to CD, *i.e.*, in this case, extension twinning can also occur, and few grains are oriented such that prism slip is required. Second, the strain response in terms of the ratio of hoop-to-axial strain can be rationalized by considering the interaction between the symmetry of the slip/twin pole figure, the initial texture and the relationship of the symmetry to loading state. For example, in axial tension and compression, the initial texture and the activity of slip are both symmetric about the loading axis and the strain ratio is close to ±0.5. However, in the case of hoop tension, the probability of grains oriented perpendicular to the loading axial is higher at the center of the pole figure than when being near the CD. Here, more strain occurs because of extension twinning in the hoop direction than in the axial direction of the tube, resulting in a hoop strain-to-axial strain ratio substantially greater than 2, *i.e.*, the initial experimental value is ≈2.8. For the case of a biaxiality ratio of 0.9, the symmetry about the loading axis is broken by the initial texture, *i.e.*, the higher probability of grains oriented near TD vs CD results in higher contribution to the macroscopic strain from the grains in the TD (or in terms of stress the hoop) orientation. This results in an experimental hoop-to-axial strain ratio of ≈2 at low strain instead of a value of unity if there had been an equal contribution of grains around the rim of the pole figure.

### B. *Texture Evolution*

The evolution of texture during deformation of magnesium is predominately controlled by $\{10\bar{1}2\}$ extension twinning which results in an 86.3-deg rotation of the basal plane around $\langle 1\bar{2}10\rangle$[3] although rotation of grains by slip can also occur. The changes in crystallographic texture observed in the current study can be rationalized by these two mechanisms. In the case of axial tension, the texture after deformation is seen in Figure 8(a) both experimentally and from VPSC simulations. The intensity of the band of grains in the TD–ND plane increases after a tensile deformation of 0.08, but the texture change is relatively small, *i.e.*, the maximum intensity increases from 1.8× to 2.7× random, while the principal features do not change. This modest strengthening of the texture can be explained by twinning of the relatively few grains found near CD and by rotation of the grains deforming predominately by basal slip toward the TD–ND plane. For a biaxiality ratio of 0.4, the situation is different from axial tension since as shown in the slip activity pole figure of Figure 8(b), a much wider range of grains near the CD orientation undergo extension twinning and grains near TD are also predicted to undergo extension twinning. For these orientations, extension twinning would cause the basal pole to rotate into the center of the pole figure. This is consistent with the strengthening of the intensity at the center observed in both the experiments and VPSC simulations.

In the case of a biaxiality ratio of 0.9, the slip activity pole figure in Figure 8(c) shows that all the grains oriented in the outer annulus of the pole figure are oriented for extension twinning. Again, the accommodation of the far field strain will cause these grains to rotate from the outer annulus to the center of the pole figure. This is consistent with the experimental and VPSC results which show a depopulation of the annulus and an increase of intensity at the center of the pole figure, *i.e.*, 4.2 and 5.2× random, respectively. The situation for hoop tension shown in Figure 8(d) is slightly different. As noted earlier for this case, the grains that show the high activity of extension twins correspond to a high intensity of grains in the initial texture. However, in this case, the 86-deg rotation due to extension twinning could orient grains anywhere along the CD–ND plane to accommodate the tensile strain in the hoop direction. This results in a band of grains along the CD–ND plane and a decrease in intensity of grains near TD consistent with the experiments and VPSC simulations.

The most dramatic change in crystallographic texture occurs for a biaxiality ratio of −0.5 and axial compression. Here the grains oriented in the band around the TD–ND plane are all oriented well for extension twinning which results in a rotation of 86 deg to orientations near the CD direction, which is again consistent with the experimental measurements in Figures 8(e) and (f) and also with the results of Jiang *et al.*[16] The one difference that can be observed between these two conditions is that the amount of twinning activity for grains oriented near the TD direction is lower in the case of a biaxiality ratio of −0.5. This is reflected in both the experimental and VPSC pole figures where the intensity at the center of the pole figure is higher than for uniaxial compression. It can be seen that in general, the experimental measurements and the VPSC simulations are in very good agreement. The VPSC simulations tend to predict somewhat stronger textures, but this is typically observed in crystal plasticity simulations.

A last point that is worth addressing is related to the evolution of texture and its effect on the change in the macroscopic strain response. It was shown earlier in Figure 6 that for biaxiality ratios of 0.4, 0.9, and hoop tension, a significant evolution of the ratio of hoop-to-axial strain occurs as the level of deformation increases. This can be related to the change in texture due to extension twinning. In Figure 6, it can be seen that the VPSC predictions for the evolution in the hoop-to-axial strain ratio reasonably capture the experimental results. However, for the case of a biaxiality ratio of 0.4, the VPSC results contradict the experimental results, *i.e.*, the plastic strain ratio decreases with deformation in the experiment, while it is predicted to increase from the VPSC simulations. The reasons for this discrepancy are not entirely clear at this point: however, it is worth noting that this condition is near the "corner" of the plastic potential where the strain normality vector is rapidly evolving. Here it may be particularly sensitive to the details of the interaction model between twinning and slip, for example.

Finally, to further test the predictive capabilities of the VPSC model, a set of biaxial tests were conducted on

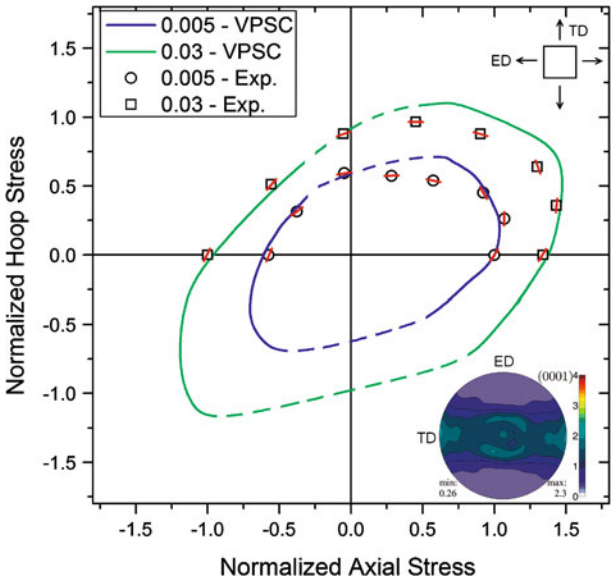


Fig. 10—Plastic potential of the extruded AZ80 for different levels of plastic deformation. The circular symbols and the blue line represent an equivalent plastic work of 0.9 MJ/m$^3$ and the square symbols represent an equivalent plastic work of 7.0 MJ/m$^3$. These levels of plastic work correspond to tensile strains in the axial direction of 0.005 and 0.03, respectively. The initial texture of the extruded material is shown by the (0001) pole inset in the bottom right corner. Note: axial stress is parallel to extrusion direction (ED) and hoop stress is perpendicular to ED.

an extruded AZ80 material. As the material came from a different supplier and had a smaller grain size than the as-cast material, the results shown in Figure 10 for the plastic response are plotted as normalized hoop and axial stresses. The starting texture is shown as insert into the figure. Here it can be observed that the extruded texture is similar to the cast crystallographic texture, *i.e.*, a band of grain orientations around the TD–ND plane, although the intensity of the texture is stronger. This can be seen not only by the higher maximum intensity of 2.3× random *vs* 1.7 times random but also in the wider range of orientations near the ED where there is a low intensity of grains. Reflecting this stronger texture, the tension/compression asymmetry for loading along ED has now increased to 1.7 and 1.4 for low and high applied strain *vs* 1.4 and 1.3 for the cast material, respectively. In general, the agreement between the experimental results and the VPSC simulations is very good with the exception of the region near biaxial tension where the simulations over-predict the combination of axial and hoop stress at both the low and higher plastic work conditions by approximately 20 pct. As noted earlier, this corresponds to the region near the "corner" of the plastic potential where the strain normality vector is rapidly evolving and the interaction between twinning and slip is strong.

## V. SUMMARY

The current study demonstrates that biaxial testing on magnesium tubular samples is an attractive technique for experimentally studying the plastic deformation over a wide range of stress states. By using a combination of axial tension or compression and internal pressure, the tension–tension and tension–compression quadrants of stress space can be carefully explored. In addition to the quantification of the axial and hoop stresses in the sample, digital image correlation can be used to provide measurements of the axial and hoop strain components. From these data, the plastic potential and its evolution with applied strain have been characterized for the magnesium alloy AZ80 for two different initial textures. It was found that even though the initial textures were relatively weak, a significant tension/compression asymmetry was observed and the shape of the plastic potential was significantly modified from an isotropic plastic potential such as von Mises. In addition, the evolution of crystallographic texture for different loading paths was characterized by pole figures determined by neutron diffraction. It was observed that the evolution of texture was strongly dependent on stress state.

The VPSC model of Tomé *et al.*[8] and the fit parameters previously determined by Jain *et al.*[9] on AZ80 were used to examine the ability of this model to predict the experimental results and also to aid in understanding the underlying deformation mechanisms, and this information could be used to rationalize the macroscopic stress–strain response and the evolution of crystallographic texture. It was found that, in general, the VPSC simulations were in close agreement with the experimental measurements for the plastic potential, the biaxial strain response, and the evolution of crystallographic texture for both the initial textures studied in the current study. However, the results from the simulations were less satisfactory in the region near biaxial tension. This was the region of the plastic potential where there was a strong competition between basal slip and extension twinning and where the strain vector was evolving very quickly as a function of the biaxial stress ratio (*i.e.*, the "corner" of the plastic potential). It is worth emphasizing that no changes were made to any of the fit parameters from the study of Jain *et al.* since one objective of the study was to examine the predictive behavior of VPSC. However, it is most likely that some modification of the input parameters could improve the predictions of VPSC in the region of biaxial tension but fundamentally there is a need for improved models to describe the behavior in this range of stress states.

## ACKNOWLEDGMENTS

The authors would like to gratefully acknowledge that this research was supported by funding from the NSERC Magnesium Strategic Research Network. More information on the Network can be found at www.MagNET.ubc.ca. The authors would also like to thank Carlos Tomé of Los Alamos National Laboratory for access to the use of the VPSC code, and K.U. Kainer, J. Bohen, and D. Letzig of the Magnesium

Innovation Centre at Helmholtz-Zentrum Geesthacht in Germany for providing the extruded AZ80 material.

## REFERENCES


1. G. Proust, C.N. Tome, and G.C. Kaschner: *Acta Mater.*, 2007, vol. 55, pp. 2137–2148.
2. S.R. Agnew: in *Advances in Wrought Magnesium Alloys: Fundamentals of Processing, Properties and Applications*, C. Bettles and M.R. Barnett, eds., 2012, Woodhead Publishing, Cambridge, U.K. pp. 63–104.
3. M.R. Barnett: in *Advances in Wrought Magnesium Alloys: Fundamentals of Processing, Properties and Applications*, C. Bettles and M.R. Barnett, eds., 2012, Woodhead Publishing, Cambridge, U.K. pp. 105–43.
4. J. Jain, J. Zou, C.W. Sinclair, and W.J. Poole: *J. Microsc.*, 2010, vol. 242, pp. 26–36.
5. U.F. Kocks and D.G. Westlake: *Trans. Metal. Soc. AIME*, 1967, vol. 239, pp. 1107–09.
6. B. Clausen, C.N. Tomé, D.W. Brown, and S.R. Agnew: *Acta Mater.*, 2008, vol. 56, pp. 2456–68.
7. S.R. Agnew, C.N. Tomé, D.W. Brown, T.M. Holden, and S.C. Vogel: *Scripta Mater.*, 2003, vol. 48, pp. 1003–08.
8. R.A. Lebensohn and C.N. Tomé: *Acta Metall. Mater.*, 1993, vol. 41, pp. 2611–24.
9. J. Jain, W.J. Poole, and C.W. Sinclair: *Mater. Sci. Eng. A.*, 2012, vol. 547, pp. 128–37.
10. H. Wang, P.D. Wu, C.N. Tomé, and Y. Huang: *J. Mech. Phys. Solids*, 2010, vol. 58, pp. 594–612.
11. A. Izadbaksh, K. Inal, and R.K. Mishra: *Modelling Simul. Mater. Sci.*, 2012, vol. 20, p. 035016.
12. S.-H. Choi, D.H. Kim, S.S. Park, and B.S. You: *Acta Mater.*, 2010, vol. 58, pp. 320–29.
13. H. Wang, B. Raeisinia, P.D. Wu, S.R. Agnew, and C.N. Tomé: *Int. J. Solids Struct.*, 2010, vol. 47, pp. 2905–17.
14. A. Jain and S.R. Agnew: *Mater. Sci. Eng. A.*, 2007, vol. 462, pp. 29–36.
15. A.A. Luo and A.K. Sachdev: in *Advances in Wrought Magnesium Alloys: Fundamentals of Processing, Properties and Applications*, C. Bettles and M.R. Barnett, eds., 2012, Woodhead Publishing, Cambridge, U.K., pp. 391–426.
16. L. Jiang, J.J. Jonas, R.K. Mishra, A.A. Luo, A.K. Sachdev, and S. Godet: *Acta Mater.*, 2007, vol. 55, pp. 3899–3910.
17. A.S. Khan, A. Pandey, T. Gnaupel-Herold, and R.K. Mishra: *Int. J. Plasticity*, 2011, vol. 27, pp. 688–706.
18. H. Wang, P.D. Wu, K.P. Boyle, and K.W. Neale: *Int. J. Solids Struct.*, 2011, vol. 48, pp. 1000–1010.
19. C.J. Neil and S.R. Agnew: *Int. J. Plasticity*, 2009, vol. 25, pp. 379–98.
20. J. Lévesque, K. Inal, K.W. Neale, and R.K. Mishra: *Int. J. Plasticity*, 2010, vol. 26, pp. 65–83.
21. S. Yi, J. Bohlen, F. Heinemann, and D. Letzig: *Acta Mater.*, 2010, vol. 58, pp. 592–605.
22. J. Kim, H. Ryou, D. Kim, W. Lee, S.-H. Hong, and K. Chung: *Int. J. Mech. Sci.*, 2008, vol. 50, pp. 1510–18.
23. M.G. Lee, S.J. Kim, R.H. Wagoner, K. Chung, and H.Y. Kim: *Int. J. Plasticity*, 2009, vol. 25, pp. 70–104.
24. M.G. Lee, R.H. Wagoner, J.K. Lee, K. Chung, and H.Y. Kim: *Int. J. Plasticity*, 2008, vol. 24, pp. 545–82.
25. D.A. Wagner, S.D. Logan, K. Wang, T. Skszek, and C.P. Salisbury: in *Magnesium Technology 2009*, 2009, TMS (The Minerals, Metals and Materials Society), San Francisco.
26. M. Geiger, M. Merklein, W. Hubnatter, and M. Gruner: *Prod. Eng. Devel.*, 2008, vol. 2, pp. 303–10.
27. S.H. Safi-Naqvi, W.B. Hutchinson, and M.R. Barnett: *Mater. Sci. Tech.*, 2008, vol. 24 (10), pp. 1283–92.
28. O. Cazacu and F. Barlat: *Int. J. Plasticity*, 2004, vol. 20, pp. 2027–45.
29. O. Cazacu, B. Plunkett, and F. Barlat: *Int. J. Plasticity*, 2006, vol. 22, pp. 1171–94.
30. B. Plunkett, O. Cazacu, and F. Barlat: *Int. J. Plasticity*, 2008, vol. 24, pp. 847–66.
31. B. Plunkett, R.A. Lebensohn, O. Cazacu, and F. Barlat: *Acta Mater.*, 2006, vol. 54, pp. 4159–69.
32. M. Li, X.Y. Lou, J.H. Kim, and R.H. Wagoner: *Int. J. Plasticity*, 2010, vol. 26, pp. 820–58.
33. S. Graff, W. Brocks, and D. Steglich: *Int. J. Plasticity*, 2007, vol. 23, pp. 1957–78.
34. F. Bachmann, R. Hielscher, and H. Schaeben: *Solid State Phen.*, vol. 160, pp. 63–68.
35. K. Pettersen, O. Lohne, and N. Ryum: *Metall. Trans. A*, 1990, vol. 21A, pp. 221–30.
36. J. Bohlen, F. Chmelik, P. Dobron, D. Letzig, P. Lukac, and K.U. Kainer: *J. Alloys Comp.*, 2004, vol. 378, pp. 214–19.
37. T. Marin, P.R. Dawson, M.A. Gharghouri, and R.B. Rogge: *Acta Mater.*, 2008, vol. 56, pp. 4183–99.
38. A. Higdon, E. Ohlsen, W.B. Stiles, J.A. Weese, and W.F. Riley: *Mechanics of Materials*, John Wiley & Sons, New York, NY, 1978.
39. B. Pan, K. Qian, H. Xie, and A. Asundi. *Meas. Sci. Techno.*, 2009, vol. 20, p. 062001 (17 pp).
40. F. Hild and S. Roux: *Strain*, 2006, vol. 42, pp. 69–80.
41. M.A. Gharghouri: Ph.D. Thesis, McMaster, 1996.
42. C. Corby, C.H. Cáceres, and P. Lukác: *Mater. Sci. Eng. A.*, 2004, vols. 387–389, pp. 22–24.
43. W.A. Backofen: *Deformation Processing*, 1972, Addison-Wesley.
44. J. Jain, W.J. Poole, C.W. Sinclair, and M.A. Gharghouri: *Scripta Mater.*, 2010, vol. 62, pp. 301–04.
45. J. Jain, W.J. Poole, and C.W. Sinclair: in *Magnesium Technology 2008*, 2008. TMS (The Minerals, Metals and Materials Society), New Orleans.
46. N. Stanford, D. Atwell, A. Beer, C. Davies, and M.R. Barnett: *Scripta Mater.*, 2008, vol. 59, pp. 772–75.